energy&fuels

pubs.acs.org/EF

Article

Fe-Doped $NaVPO_4F$/C Compounds for Sodium-Ion Battery Cathodes: Electrochemical Performance and Analysis of Kinetic Properties

Kang Tang, Hualing Tian, Yanhui Zhang, Yanjun Cai, He Ren, Yingbo Wang, Xiang Yao,* and Zhi Su*

Cite This: *Energy Fuels* 2024, 38, 18035−18043

Read Online

ACCESS | Metrics & More | Article Recommendations | Supporting Information

ABSTRACT: NASICON-type $NaVPO_4F$ (NVPF) has received much attention from researchers due to its open three-dimensional framework and high theoretical capacity. However, the limited internal electronic conductivity and energy density hinder the widespread commercialization of NVPF. Herein, a series of $NaV_{1-x}Fe_xPO_4F$/C (x = 0, 0.04, 0.06, and 0.08) was constructed via a sol−gel method by introducing a partial amount of Fe^{3+} into NVPF. The introduction of Fe^{3+} doping effectively enhanced the structural stability of the material, thereby facilitating rapid Na^+ intercalation/deintercalation and leading to improved electrochemical properties. The results show that NVPF−$Fe_{0.06}$ has excellent electrochemical performance, with a discharge specific capacity of 133.8 mAh g^{-1} at 0.2 C and a capacity retention of 94.5% after 100 charge/discharge cycles. Even after 1000 cycles at 5 C, it still has a high capacity retention of 86.2%. Additionally, the de-embedding mechanism of the NVPF−$Fe_{0.06}$ electrode material is revealed by *ex situ* X-ray diffraction and *in situ* electrochemical impedance spectroscopy results. More importantly, the specific discharge capacity of assembled HC//NVPF−$Fe_{0.06}$ full cell reached 112.1 mAh g^{-1} at 5 C. This work explores a new avenue to facilitate the commercialization of polyanionic cathode materials.

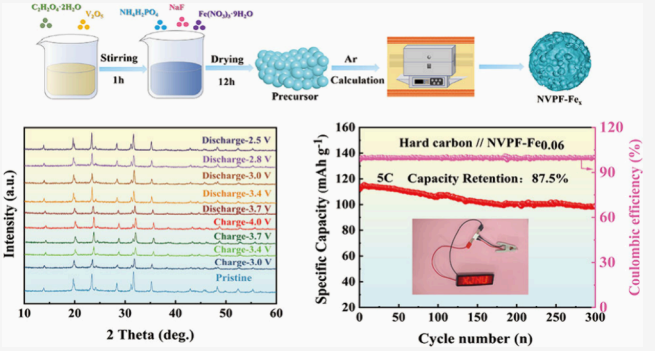

1. INTRODUCTION

In recent decades, lithium-ion batteries (LIBs) have successfully penetrated the new energy market and become an integral part of everyday life due to their high energy density and excellent cycle stability.[1] However, the lithium resource reserves are exceedingly limited, leading to a substantial increase in the cost of lithium.[2] Sodium metal is not only abundant and inexpensive, but lithium and sodium also belong to the same main group and have similar physicochemical properties.[3] This means that research efforts related to LIBs can be derived directly from sodium-ion batteries (SIBs), making them a strong contender for next-generation large-scale energy storage systems.[4,5] The low energy density of SIBs is attributed to the substantial radius and weight of sodium atoms.[6] In SIBs, selecting the cathode material is crucial for achieving high battery energy density.[7,8] Up now, the cathode materials with excellent potential are mainly categorized into transition metal oxide compounds, Prussian blue analogues, and polyanionic compounds.[9−15]

Among various materials, the NASICON-type polyanionic compound $NaVPO_4F$ (NVPF) has attracted widespread attention due to its strong covalent P−O bond, which is conducive to slowing the structural evolution during the Na^+ deposition process.[16] Moreover, the introduction of strong electronegative F^- in the system can further improve the working voltage.[17,18] At the same time, $NaVPO_4F$ has a high theoretical capacity (143 mAh g^{-1})[19] and low content of toxic vanadium compared to other phosphate compounds $Na_3V_2(PO_4)_3$ (117.6 mAh g^{-1})[20] and $Na_3V_2(PO_4)_2F_3$ (128 mAh g^{-1}),[21] thus making NVPF become a high-performance green cathode material with excellent development prospects. However, the low internal electronic conductivity of NVPF is only 3.9−6.2 × 10^{-12} S cm^{-1}, which makes its long cycle and rate performance much lower than expected.[22] Therefore, NVPF is difficult to apply in commercial applications. To solve this problem, many methods have been applied to modify electrode materials, such as composite carbon materials with good conductivity,[23−26] nanostructure design,[27] and ion doping (Al^{3+},[28] W^{6+},[29] and Ti^{4+} [30]). Furthermore, composite carbon materials entail higher costs.[31] However, ion doping is widely favored by researchers as an economically viable and environmentally friendly strategy.[32] Wang et al. reported that the introduction of Zr^{4+} into $Na_4MnV(PO_4)_3$/C enlarged the lattice volume and facilitated the Na^+ transport, resulting in a

Received: June 4, 2024
Revised: August 20, 2024
Accepted: August 22, 2024
Published: September 2, 2024

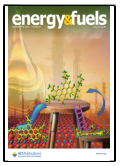

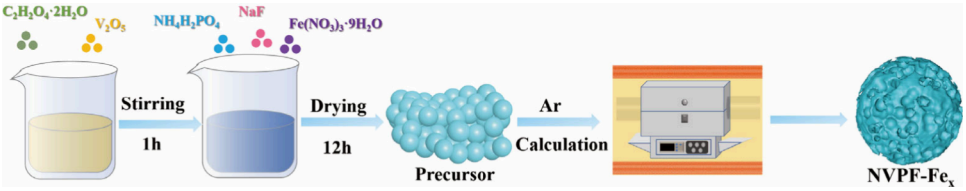

Figure 1. Schematic flowchart of the preparation of sample NVPF−Fe_x.

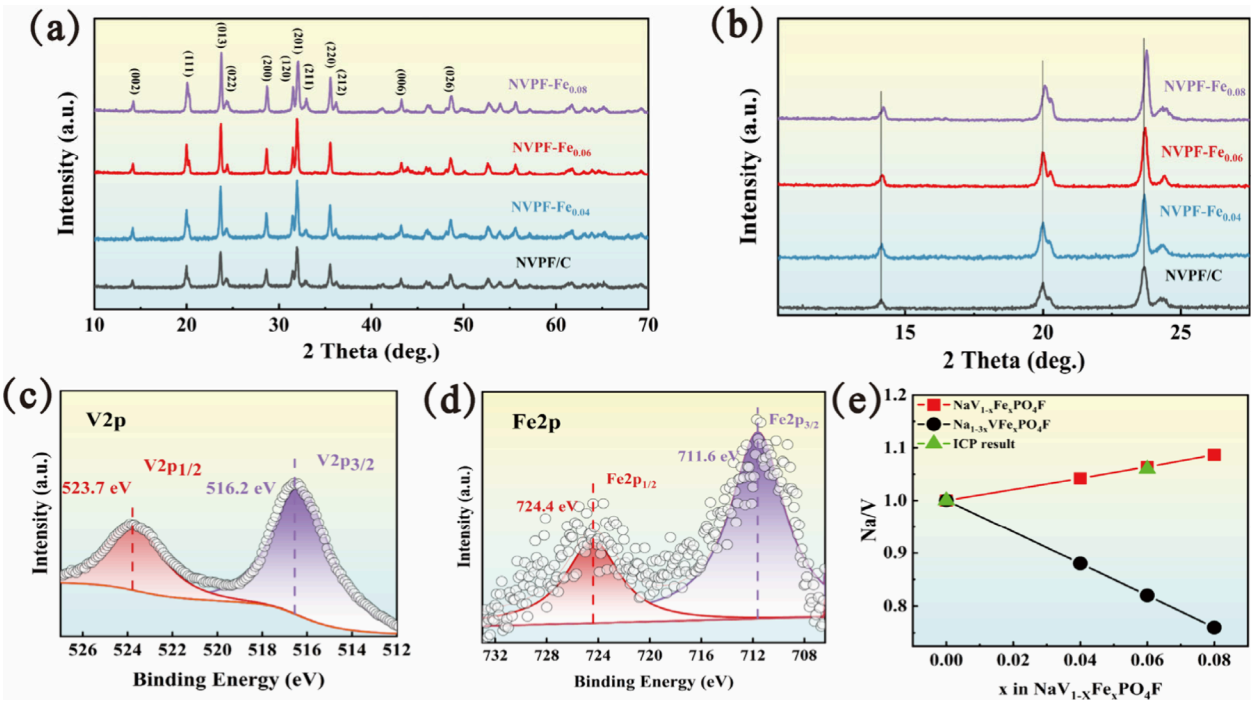

Figure 2. (a) XRD patterns of the synthesized NVPF−Fe_x (x = 0, 0.04, 0.06, and 0.08) samples. (b) Local enlargement of the XRD pattern. (c and d) V 2p and Fe 2p of the NVPF−$Fe_{0.06}$ sample. (e) Na/V ratio for NVPF−Fe_x obtained from the ICP analysis and various models listed in the legend.

high capacity retention of 81.2% for $Na_{3.9}Mn_{0.95}Zr_{0.05}V(PO_4)_3$/C samples after cycling at 1 C for 500 cycles.[33] Chen et al. reported that the addition of Ga^{3+} to $Na_3V_2(PO_4)_3$ activated additional redox pairs (V^{4+}/V^{5+}) at 4 V, resulting in an increased energy density that exceeded the theoretical specific capacity by 152.3 mAh g^{-1} at 1 C. Furthermore, even at 20 C, the material exhibited minimal capacity loss with a rate of only 0.02375% per cycle after 1000 cycles.[34] Yue et al. synthesized $Na_3V_{1.85}Fe_{0.15}(PO_4)_2O_2F$ microcubes by substituting some of V^{3+} with Fe^{3+}, resulting in an outstanding discharge specific capacity of 137.2 mAh g^{-1} at 1 C. The reason for the improved performance is that Fe doping improves the internal conductivity of NVFPOF and slows the rate of structural evolution during the cycle.[35]

Fe is not only cheap with large reserves, but Fe^{3+} also has a small ionic radius (0.64 Å) can enter the V^{3+} (0.74 Å) site easily. Herein, in this work, Fe^{3+} was successfully doped into $NaVPO_4F$, replacing a portion of V^{3+} to construct a series of $NaV_{1-x}Fe_xPO_4F$/C (x = 0, 0.04, 0.06, and 0.08 hereafter referred to as NVPF/C and NVPF−Fe_x) materials synthesized by a sol−gel method. The results demonstrate that NVPF−$Fe_{0.06}$ displays outstanding electrochemical properties due to a 2−3 nm thick amorphous carbon layer on its surface. Furthermore, many irregular perforations are formed on the material's surface, enlarging the Na^+ transmission pathway and significantly enhancing the material's internal electronic conductivity. Additionally, introducing Fe^{3+} doping can enhance the stability of the crystal structure and effectively improve the material's structural reversibility during cycling. The sodium deintercalation mechanism of NVPF−$Fe_{0.06}$ during charge and discharge was observed by *ex situ* X-ray diffraction (XRD) and *in situ* electrochemical impedance spectroscopy (EIS). Moreover, the specific discharge capacity of the HC//NVPF−$Fe_{0.06}$ full cell was 112.1 mAh g^{-1} at 5 C, further demonstrating the good potential of the Fe^{3+} doping strategy.

2. EXPERIMENTAL SECTION

2.1. Material Synthesis. $NaV_{1-x}Fe_xPO_4F$/C (x = 0.04, 0.06, and 0.08) was synthesized via the sol−gel method followed by high-temperature calcination. A total of 3 mmol of V_2O_5 and 11 mmol of $H_2C_2O_4·2H_2O$ were added to the beaker and stirred at 70 °C for 1 h. The mixture was then supplemented with 3 mmol of NaF, 3 mmol of $NH_4H_2PO_4$, and a specific quantity of $Fe(NO_3)_3·6H_2O$, followed by stirring for 5 h to yield a dark green gel. Subsequently, the gel was subjected to drying at 90 °C for 12 h. The precursor was heat-treated in a tube furnace at 350 °C in an argon atmosphere for 4 h, and then the temperature was raised to 750 °C for calcination for 8 h to obtain the target product NVPF−Fe_x (x = 0.04, 0.06, and 0.08). The preparation process of NVPF/C samples was the same as that above, without adding $Fe(NO_3)_3·6H_2O$.

https://doi.org/10.1021/acs.energyfuels.4c02693
Energy Fuels 2024, 38, 18035−18043

2.2. Material Characterization. The crystal structure of the sample was characterized by XRD (Bruker D2, Cu Kα). The microstructure of the sample was analyzed using scanning electron microscopy (SEM, Thermo Scientific Apreo 2C) and high-resolution transmission electron microscopy (HR-TEM, Talos F200S G2). The pore type of the material was determined by an automatic physical adsorption instrument [Brunauer–Emmett–Teller (BET), ASAP 2020 Plus]. The carbonized sample's graphitization degree was analyzed using Raman spectroscopy (Thermo Scientific DXR3xi). The valence states and elemental proportions were determined using X-ray photoelectron spectroscopy (XPS, Thermo Scientific K-Alpha X) and inductively coupled plasma optical emission spectrometry (ICP–OES, PE Avio 200). Electronic conductivity of the sample is made by the four-point probe method.

2.3. Electrochemical Measurement. The manufacturing of the active pole piece is by mixing the active material, acetylene black, and polyvinylidene fluoride under the mass ratio of 8:1:1 and then dropping *N*-methylpyrrolidone as a sol. After fully ground and mixed, the slurry is evenly coated on the aluminum foil. In addition, the aluminum foil is transferred to the vacuum drying oven at 80 °C for 12 h. After drying, it is cut into a circular pole sheet with a diameter of 12 mm, and the active material loading of the pole sheet is approximately 2.0 mg cm^{-1}. The CR2032 button half-cell assembly in the glovebox is full of high-purity argon gas after the completion of the assembly stands for 12 h. On the LAND battery test system (CT2100A), the half battery is subjected to a constant current charge and discharge (GCD) test. Cyclic voltammetry (CV) curves and electrochemical impedance spectroscopy (EIS) were determined by a CHI760E electrochemical workstation. The full battery is assembled with hard carbon as the anode material and NVPF–$Fe_{0.06}$ as the cathode material. Hard carbon was obtained by assembling a half-cell battery with sodium as the counterelectrode at a current density of 30 mA g^{-1} after 3 charge and discharge cycles.

3. RESULTS AND DISCUSSION

Figure 1 shows the NVPF–Fe_x sample preparation process. Oxalic acid and V_2O_5 are added to the beaker. Oxalic acid not only provides an acidic and reducing environment but also acts as a carbon source, which is wrapped on NVPF–Fe_x to form an amorphous carbon layer. Next, $NH_4H_2PO_4$, NaF, and $Fe(NO_3)_3{\cdot}6H_2O$ are added as a phosphorus source, sodium source, and iron source, respectively. After the water evaporates, the dark green gel is obtained. The sample is then calcined in a tubular furnace to obtain NVPF–Fe_x.

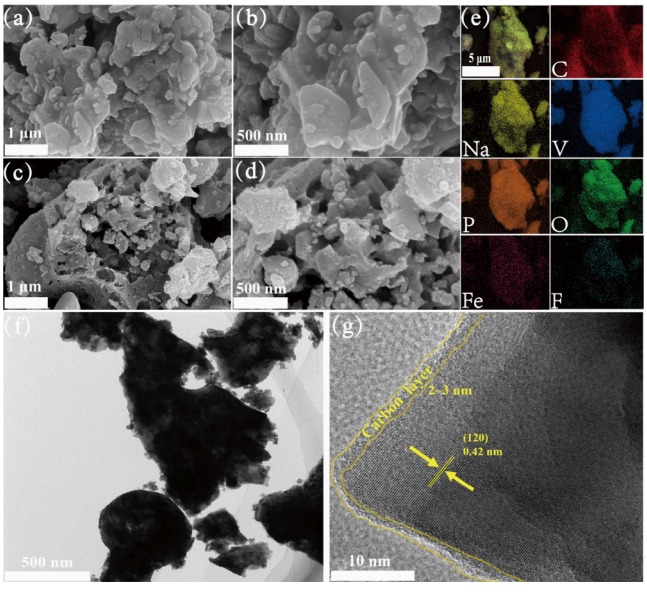

Figure 3. SEM images of (a and b) NVPF/C and (c and d) NVPF–$Fe_{0.06}$. (e) EDS mapping image of NVPF–$Fe_{0.06}$. (f and g) TEM images of NVPF–$Fe_{0.06}$.

The XRD pattern of each sample of NVPF–Fe_x is shown in Figure 2a. The samples obtained are highly crystalline with all diffraction peaks typical of NASICON monoclinic crystals in space group *C*2/*c*, as reported in the literature.[36,37] In addition, no additional impurity peak is detected with the increase of Fe^{3+} doping, indicating that Fe^{3+} doping does not alter the crystal structure of NVPF. From the locally enlarged XRD pattern in Figure 2b, it is evident that the crystal diffraction peak has shifted toward a higher 2θ angle, because the ionic radius of Fe^{3+}(0.64 A) is smaller than that of V^{3+}(0.74 A). The XPS analysis in Figure 2c reveals that the V $2p_{1/2}$ and V $2p_{3/2}$ peaks are observed at binding energies of 523.7 and 516.2 eV, respectively, indicating the presence of vanadium in the +3 oxidation state.[34] In Figure 2d, two peaks at 724.4 and 711.6 eV were observed in the NVPF–$Fe_{0.06}$ sample, corresponding to Fe $2p_{1/2}$ and Fe $2p_{3/2}$, respectively, revealing successful doping of Fe^{3+} into the NVPF–$Fe_{0.06}$ sample.[38] This result demonstrates that minor Fe doping has little effect on the chemical valence state of V. In addition, Na 1s, F 1s, O 1s, C 1s, and P 2p were detected in the full spectrum of XPS in NVPF–$Fe_{0.06}$ samples (Figure S1 of the Supporting Information). The Raman spectra exhibit two distinct peaks at wavenumbers of 1341 and 1587 cm^{-1}, corresponding to the D peak (defect induced) and G peak (crystalline graphite) (Figure S2 of the Supporting Information). The intensity ratios I_D/I_G of NVPF–Fe_x (x = 0, 0.04, 0.06, and 0.08), are 1.12, 1.11, 1.17, and 1.15, respectively. The similar I_D/I_G value simply indicates that the Fe doping has no significant impact on the graphitization degree of the carbon layers. Moreover, the high I_D/I_G values reveal that carbon is amorphous in nature.[39] Tables S1 and S2 of the Supporting Information show the theoretical Na/V ratios of Fe doping at the V site and Fe doping at the Na site, respectively. Actual ICP measurement results are shown in Table S3 of the Supporting Information. The comparison of the Na/V ratio trends for different doping sites is displayed in Figure 2e. It is found that the Na/V ratio trend from ICP is consistent with the theoretical value of Na/V ratio (Fe^{3+} is doped on the V site).[40] The V and Fe contents of NVPF–$Fe_{0.06}$ sample were measured by ICP–OES, and the results were in general agreement with the set values of 0.936:0.064 and 0.94:0.06.

The morphology and microstructure of the NVPF–Fe_x samples were observed by SEM and HR-TEM. Panels a–d of Figure 3 show that NVPF samples are irregularly distributed and agglomerated. On the contrary, an irregular porous structure was formed on the surface of NVPF–$Fe_{0.06}$, allowing for increased Na^+ transport channels. The pore morphology and size of NVPF–$Fe_{0.06}$ were characterized by analyzing the nitrogen adsorption and desorption isotherms. As shown in Figure S3 of the Supporting Information, the isotherm curve belongs to the typical class IV Langmuir isotherm with obvious hysteresis and pore size between 19.2 and 31.8 nm, indicating that it belongs to mesoporous materials. A trace amount of pores is generated on the surface of NVPF–$Fe_{0.04}$, while the pores on the surface of NVPF–$Fe_{0.08}$ completely disappear, as shown in Figure S4 of the Supporting Information. The mapping image (Figure 3e) demonstrates the uniform distribution of the Na, V, Fe, P, O, F, and C elements in the NVPF–$Fe_{0.06}$ sample. The HR-TEM image in panels f and g of Figure 3 reveals that the surface of NVPF–$Fe_{0.06}$ is coated with

https://doi.org/10.1021/acs.energyfuels.4c02693
Energy Fuels 2024, 38, 18035–18043

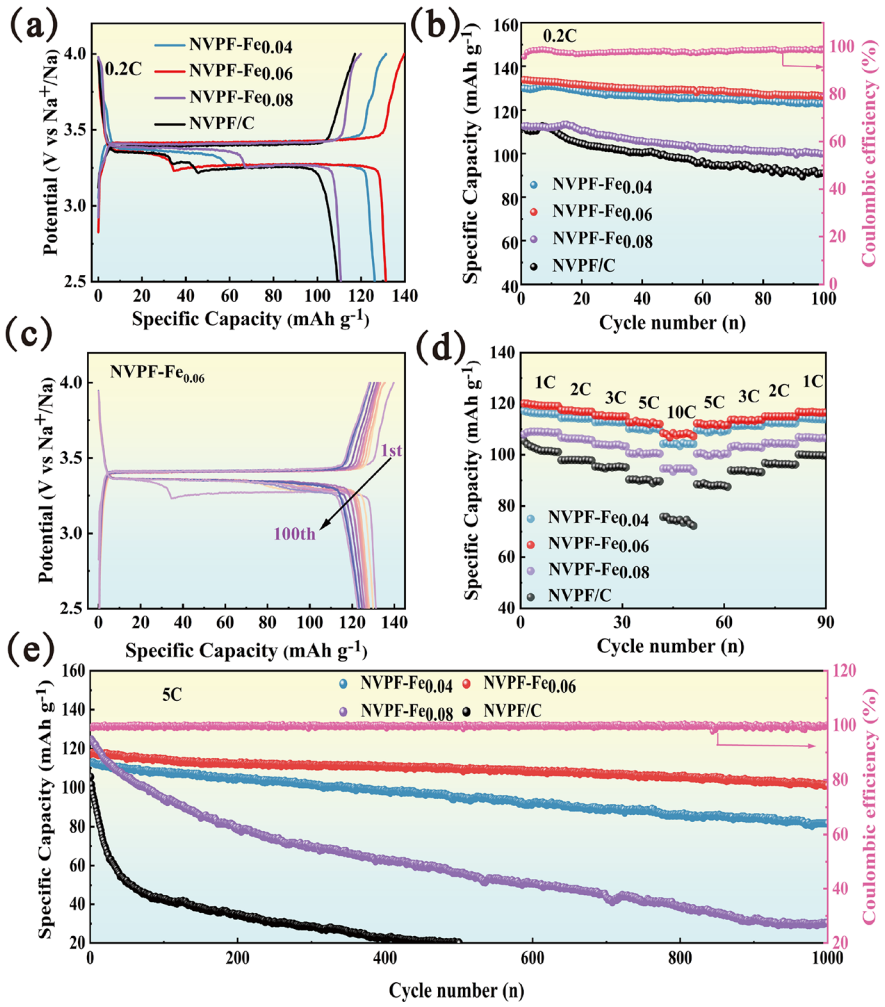

Figure 4. Electrochemical performances of NVPF−Fe$_x$. (a) Initial GCD curves. (b) Cyclic and (c) voltage curves through different charge and discharge cycles. (d) Rate performance. (e) Long cycle stability of NVPF−Fe$_x$ (x = 0, 0.04, 0.06, and 0.08) at 5 C for 1000 cycles.

a 2−3 nm thick layer of amorphous carbon, and the uniform distribution of this carbon layer facilitates enhanced electron transport speed. The crystal spacing is 0.42 nm, corresponding to the (120) crystal face of the NVPF−Fe$_{0.06}$ sample.[41]

The electrochemical properties of NVPF−Fe$_x$ (x = 0, 0.04, 0.06, and 0.08) were studied by assembling CR2032 half cells. Figure 4a illustrates the GCD test at 0.2 C within a voltage range of 2.5−4.0 V. All samples exhibited a broad charge/discharge plateau around 3.4 V, corresponding to a reversible redox reaction of V^{3+}/V^{4+}.[41] The discharge curves of all of the samples showed a voltage step phenomenon; it arises due to an *in situ* passivation layer formed on the sodium counter-electrode caused by solvent [ethylene carbonate (EC)/dimethyl carbonate (DMC)] interactions that produce surface species, which form and dissolve during each cycle. However, when diethylene glycol dimethyl ether (DIGLYME) is used as the solvent, no second discharge platform appears (Figure S5a of the Supporting Information). For the electrolyte with DIGLYME as the solvent, the voltage curve of 10 cycles at 0.2 C is shown in Figure S5b of the Supporting Information, and the second voltage platform does not appear. Therefore, it can be considered that the reason for the formation of the second discharge platform is the *in situ* passivation layer formed by the EC/DMC solvent on the sodium electrode, which has nothing to do with the properties of the material itself.[43,44] The specific capacity of NVPF−Fe$_{0.06}$ was 133.8 mAh g^{-1}, significantly surpassing that of NVPF/C, NVPF−Fe$_{0.04}$, and NVPF−Fe$_{0.08}$ at 112.1, 129.9, and 112.6 mAh g^{-1} respectively. After 100 cycles, NVPF−Fe$_{0.06}$ exhibited the highest capacity retention of 94.5%, whereas NVPF/C achieved only 82.0% (Figure 4b). From the selected GCD curves, NVPF−Fe$_{0.06}$ exhibits high voltage as well as high capacity retention after 100 cycles (Figure 4c). Figure 4d shows the rate performance of NVPF−Fe$_x$ at 1, 2, 3, 5, and 10 C, respectively. NVPF−Fe$_{0.06}$ exhibits excellent reversible capacities of 119.9, 117.5, 115.4, 113.2, and 108.4 mAh g^{-1} at different rates at 1, 2, 3, 5, and 10 C and quickly recovers to 116.7 mAh g^{-1} when returning to 1 C. At the same time, NVPF/C has a lower reversible discharge capacity of only 72.3 mAh g^{-1} at 10 C. As shown in Figure S6 of the Supporting Information, the GCD curves of NVPF−Fe$_{0.06}$ at different rates have a better overlap compared to NVPF/C, which exhibits a smaller polarization tendency and high capacity retention. As shown in Figure S7 of the Supporting Information, even at 15, 20, and 25 C, the specific discharge capacity of x = 0.06 is the highest at 107.8, 103.3, and 98.3 mAh g^{-1} compared to x = 0.04 and 0.08. Additionally, to investigate the long-cycle stability of the material, the results after 1000 cycles at 5 C are shown in Figure 4e. NVPF−Fe$_{0.06}$ still exhibits a favorable discharge capacity of 117.2 mAh g^{-1}, with a capacity retention of 86.2%, and maintains a coulombic

https://doi.org/10.1021/acs.energyfuels.4c02693
Energy Fuels 2024, 38, 18035−18043

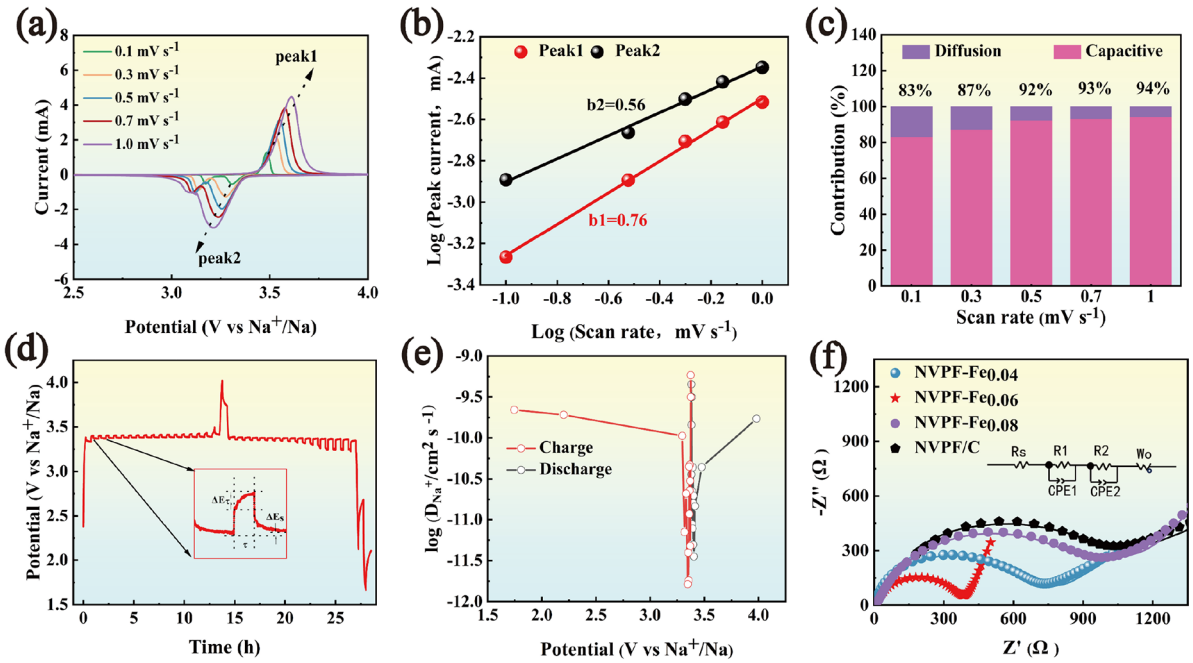

Figure 5. (a) Different scanning rates CV of NVPF−$Fe_{0.06}$ samples. (b) Linear fittings of log(*i*, peak current) versus log(*v*, scan rate). (c) Pseudocapacitive contribution of NVPF−$Fe_{0.06}$ at various scan rates. (d) Voltage profile during GITT for the NVPF−$Fe_{0.06}$ sample. (e) Apparent diffusion coefficients of Na^+ from the GITT profiles. (f) Nyquist plot of NVPF−Fe_x.

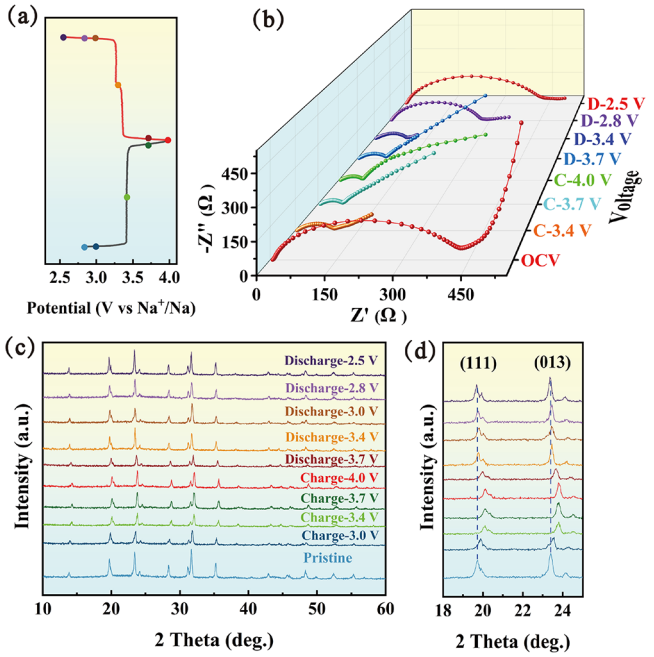

Figure 6. (a) Charge−discharge curves of the NVPF−$Fe_{0.06}$ battery in the first cycles at 0.2 C. (b) *In situ* EIS profile. (c) *Ex situ* XRD profile. (d) XRD curves in partially selected areas.

efficiency of approximately 100%. NVPF−$Fe_{0.04}$ and NVPF−$Fe_{0.08}$ have capacity retention of 72.5 and 24.5%, respectively. However, the capacity of NVPF/C has decreased to 0 at about 500 cycles, owing to the structural instability and poor reversibility of NVPF/C. The NVPF−$Fe_{0.06}$ cathode material was XRD-tested by detachment after 1000 cycles at 5 C. The results are shown in Figure S8 of the Supporting Information, after a long time of cycling, and the peak shape and intensity of NVPF−$Fe_{0.06}$ remain largely unchanged, suggesting that the doping of Fe^{3+} can effectively improve the structural stability of the material.[35] The outstanding electrochemical performance of NVPF−$Fe_{0.06}$ can be attributed to the doping of Fe^{3+} at an appropriate concentration, which enhances the crystal structure stability of the material and facilitates an efficient and stable Na^+ shuttle through the structure.[45] Additionally, the material is coated with a highly conductive carbon layer and formed a porous structure, significantly expanding the transmission path of Na^+, leading to an enhanced internal electronic conductivity of the material. Moreover, the conductivity of NVPF−$Fe_{0.06}$ was determined to range from 1.4×10^{-3} to 8.2×10^{-3} S cm^{-1} using the four-point probe method (Figure S9 of the Supporting Information). The electronic conductivity of the material has achieved a higher value compared to the previously reported range of $3.9–6.2 \times 10^{-12}$ S cm^{-1}.[22]

To study the effect of Fe^{3+} doping on the dynamic properties of NVPF, CV tests were conducted at a scanning rate of 0.1 mV s^{-1} in the voltage range of 2.5−4.0 V, and the results were shown in Figure S10 of the Supporting Information. Both NVPF/C and NVPF−$Fe_{0.06}$ electrodes exhibit a pair of characteristic peaks around 3.4 V, coinciding with the charge/discharge platform position on the GCD curve, representing to the V^{3+}/V^{4+} redox pair. The mechanism of the de-embedding reaction of Na^+ can be described as follows: $NaVPO_4F \leftrightarrow Na_{1-x}VPO_4F + xNa^+ + xe^-$, where $0 < x \leq 1$.[41] The peak potential difference of 0.16 V for NVPF−$Fe_{0.06}$ is significantly lower than that of 0.29 V for NVPF/C. The peak shape of the redox peak is also sharper, suggesting that NVPF−$Fe_{0.06}$ is less electrochemically polarized and more electrochemically reversible, resulting in faster Na^+ de-embedding kinetics.[46] In addition, a cleavage phenomenon was observed at the reduction peak around 3.4 V, and it could be attributed to the transfer of Na^+ from the Na(1) site to the Na(2) site due to the localized temperature increase during the charging and discharging process.[47−49]

https://doi.org/10.1021/acs.energyfuels.4c02693
Energy Fuels 2024, 38, 18035−18043

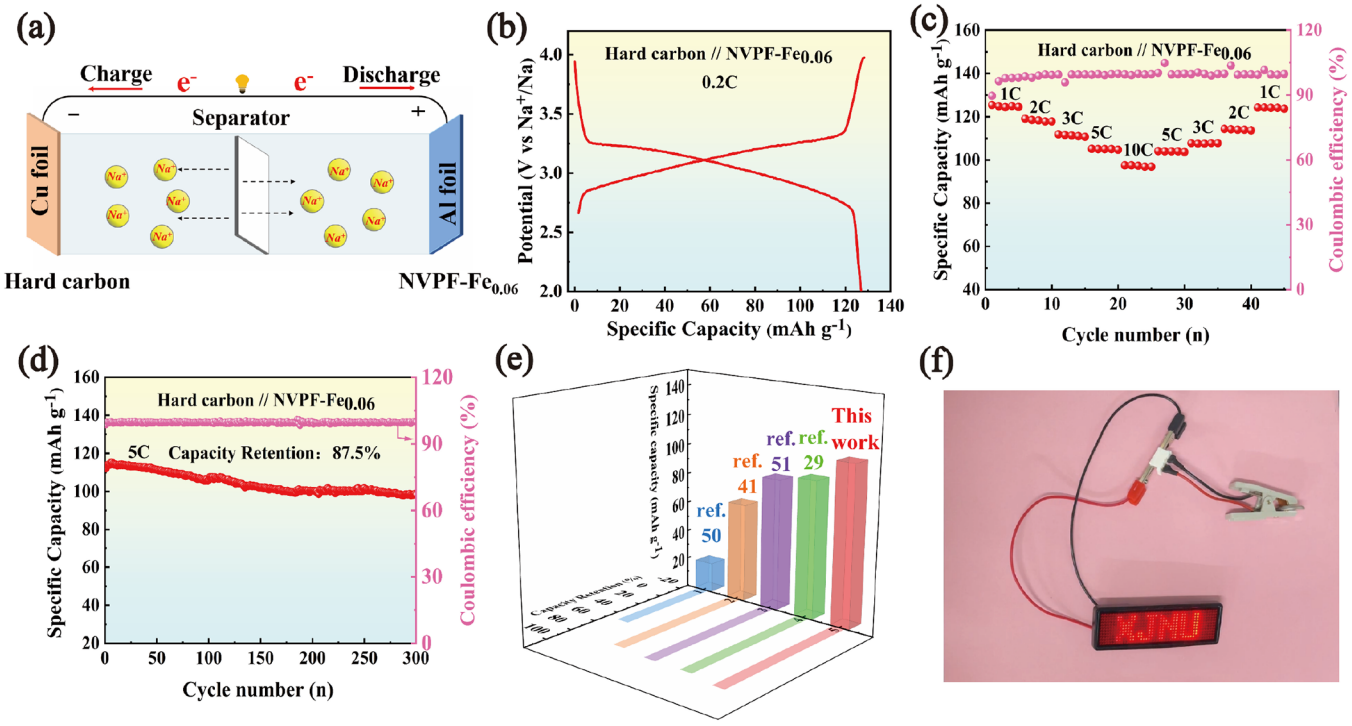

Figure 7. (a) Schematic illustration of the HC//NVPF−$Fe_{0.06}$ full cell. (b) GCD curves at 0.2 C. (c) Rate capabilities from 1 to 10 C. (d) Cyclic performance. (e) Comparison of electrochemical properties to recent literature results. (f) Digital photos of LED bulbs powered by a full cell.

To further clarify the reasons for the improvement of the electrochemical performance after Fe^{3+}, the multi-sweep CV study on the kinetic characteristics of NVPF−$Fe_{0.06}$ was conducted, as shown in Figure 5a. In general, the peak current and sweep speed satisfy the following relation:[50]

$$i = av^b \tag{1}$$

To further evaluate the contribution of diffusion control and capacitance control at different scan rates, eq 1 can be divided into

$$i(v) = k_1 v + k_1 v^{1/2} \tag{2}$$

$k_1 v$ and $k_1 v^{1/2}$ account for the capacitive and diffusive behaviors, respectively. The capacitive behavior of the material reflects the multiplicative performance of the material, while the diffusive behavior reflects the cyclic performance of the material. The values of a and b depend upon the type of capacity contribution, and the values of b shown by Figure 5b are 0.56 and 0.76, indicating that both capacitive and diffusive behaviors are present in NVPF−$Fe_{0.06}$. At a scan rate of 1.0 mV s^{-1}, the contribution of NVPF−$Fe_{0.06}$ to the overall capacitance behavior of 94% is significantly higher than that of NVPF/C (68%), as shown in Figure 5c and Figure S11 of the Supporting Information. Figure S12 of the Supporting Information shows D_{Na^+} of the sample obtained according to the calculation results, and the D_{Na^+} values of NVPF/C and NVPF−$Fe_{0.06}$ are 4.76×10^{-10} and 1.15×10^{-8} cm^2 s^{-1}, respectively.[51,52] The findings indicate that Fe^{3+} doping significantly enhances the capacitive behavior of NVPF, resulting in an outstanding rate performance. The apparent Na^+ diffusion coefficient of NVPF−$Fe_{0.06}$ was further determined by the constant current titration technique (GITT), as shown in the calculation procedure and the voltage profiles (Figure 5d and Figure S13 of the Supporting Information). NVPF−$Fe_{0.06}$ exhibits faster transfer kinetics of D_{Na^+} ($10^{-9.2}$−$10^{-11.7}$ cm^2 s^{-1}) compared to that of NVPF/C ($10^{-9.3}$−$10^{-13.1}$ cm^2 s^{-1}). Furthermore, as shown in Figure 5f and Table S4 of the Supporting Information, NVPF−$Fe_{0.06}$ exhibits a lower charge transfer resistance (R_{ct}) compared to NVPF/C (385.6 Ω versus 1057.3 Ω), providing further evidence of the exceptional electronic conductivity and enhanced Na^+ transport speed of NVPF−$Fe_{0.06}$.

The electrode behavior during charging and discharging was further investigated using *in situ* EIS and *ex situ* XRD. Figure 6a illustrates the first cycle charge and discharge curves of the NVPF−$Fe_{0.06}$ electrode. As depicted in Figure 6b, at an open circuit potential, the R_{ct} value is 430.4 Ω. Throughout the charging process, the semicircle diameter of the high-frequency region continuously decreases, reaching a value of 63.2 Ω at a charge of 4 V, which may be attributed to Na^+ extraction of $NaVPO_4F \rightarrow Na_{1-x}VPO_4F + xNa^+ + xe^-$. Subsequently, upon entering the discharge stage and with the embedding of Na^+, the R_{ct} value began to rise continuously until it reached 432.8 Ω at a voltage of 2.5 V, corresponding to the reaction $Na_{1-x}VPO_4F + xNa^+ + xe^- \rightarrow NaVPO_4F$. In addition, *ex situ* XRD tests were performed on the cells to investigate the possible structural evolution of NVPF−$Fe_{0.06}$ during the charging and discharging processes. Figure 6c shows the first cycle *ex situ* XRD pattern of NVPF−$Fe_{0.06}$ at 0.2 C. All diffraction peaks in the XRD pattern are consistent with Figure 2a, which belongs to the monoclinic crystal system. The changes in the diffraction peaks of (111) and (013) were chosen to probe the structural evolution during cycling (Figure 6d). With the process of charging, the diffraction peaks of 19.7° and 23.4° gradually weaken, and the diffraction peaks shift toward a higher angle, which may be due to the lattice shrinkage caused by the departure of Na^+. When the battery was charged to the maximum voltage of 4 V, the intensity and position of the peak did not change significantly, indicating

https://doi.org/10.1021/acs.energyfuels.4c02693
Energy Fuels 2024, 38, 18035−18043

that a stable intermediate $Na_{1-x}VPO_4F$ was obtained when Na^+ was removed. In the process of discharge, due to the lattice expansion caused by the insertion of Na^+, the diffraction peak moves to a lower angle. At the end of the discharge, the crystal structure changes back to the original monoclinic $NaVPO_4F$ phase, indicating that the sodium ion embedding and de-embedding reaction is reversible.[53]

To verify the practicality of the NVPF−$Fe_{0.06}$ cathode material, the full cell was assembled as shown in Figure 7a. In addition, HC and sodium metal assembled into a battery showed representative electrochemical performance (Figure S14 of the Supporting Information). Figure 7b shows the GCD curve of HC//NVPF−$Fe_{0.06}$ at 0.2 C. A clear charge/discharge platform is observed at approximately 3.4 V, corresponding with the findings of the half-cell experiment. The initial discharge capacity was 127.0 mAh g^{-1}, which remained high capacity of 122.1 mAh g^{-1} after 50 cycles (Figure S15 of the Supporting Information). In addition, HC//NVPF−$Fe_{0.06}$ showed high specific discharge capacities of 124.9, 118.5, 111.6, 105.1, and 97.3 mAh g^{-1} at 1, 2, 3, 5, and 10 C, respectively (Figure 7c). Even at 5 C, the discharge specific capacity of HC//NVPF−$Fe_{0.06}$ was 112.1 mAh g^{-1}, and the capacity retention after 300 cycles is 87.5% (Figure 7d). In comparison to the currently reported NVPF materials, the full cell has advantages in terms of electrochemical performance (Figure 7e).[29,42,54,55] At the same time, Figure 7f shows that the HC//NVPF−$Fe_{0.06}$ full battery lights up the light-emitting diode (LED) bulb, indicating that the NVPF−$Fe_{0.06}$ cathode material has a great practical application value.

4. CONCLUSION

In summary, $NaV_{1-x}Fe_xPO_4F/C$ (x = 0, 0.04, 0.06, and 0.08) cathode materials were successfully prepared by the sol−gel method. In addition, the obtained NVPF−$Fe_{0.06}$ cathode materials exhibit excellent electrochemical performance. NVPF−$Fe_{0.06}$ has a discharge specific capacity of 133.8 mAh g^{-1} at 0.2 C, and a capacity retention of 94.5% after 100 cycles, which also maintains a high capacity of 98.3 mAh g^{-1} at 25 C. More importantly, the specific discharge capacity of assembled HC//NVPF−$Fe_{0.06}$ full cell reached 112.1 mAh g^{-1} at 5 C. NVPF−$Fe_{0.06}$ is encapsulated by a uniformly distributed carbon layer, forming an irregular porous structure on the material's surface. This effectively increases the diffusion channel of Na^+ and results in an electronic conductivity of 1.4−8.2 × 10^{-3} S cm^{-1}, significantly improving Na^+ transport kinetics. Moreover, Fe^{3+} can strongly increase the structural stability of NVPF, which makes the structural evolution of NVPF highly reversible during the charging and discharging process, as observed by *ex situ* XRD and *in situ* EIS. The straightforward and cost-effective approach can efficiently fabricate high energy density cathode materials for SIBs.

■ ASSOCIATED CONTENT

Supporting Information

The Supporting Information is available free of charge at https://pubs.acs.org/doi/10.1021/acs.energyfuels.4c02693.

Characterization details, electrochemical performance, and relevant table data (PDF)

■ AUTHOR INFORMATION

Corresponding Authors

Xiang Yao − *College of Chemistry and Chemical Engineering, Xinjiang Key Laboratory of Energy Storage and Photoelectroctalytic Materials, Xinjiang Normal University, Urumqi, Xinjiang 830054, People's Republic of China;* orcid.org/0000-0002-9948-3879; Email: yaoxiangxjnu@163.com

Zhi Su − *College of Chemistry and Chemical Engineering, Xinjiang Key Laboratory of Energy Storage and Photoelectroctalytic Materials, Xinjiang Normal University, Urumqi, Xinjiang 830054, People's Republic of China; Xinjiang University, Urumqi, Xinjiang 830046, People's Republic of China;* orcid.org/0000-0001-7310-8176; Email: suzhixj@163.com

Authors

Kang Tang − *College of Chemistry and Chemical Engineering, Xinjiang Key Laboratory of Energy Storage and Photoelectroctalytic Materials, Xinjiang Normal University, Urumqi, Xinjiang 830054, People's Republic of China*

Hualing Tian − *College of Chemistry and Chemical Engineering, Xinjiang Key Laboratory of Energy Storage and Photoelectroctalytic Materials, Xinjiang Normal University, Urumqi, Xinjiang 830054, People's Republic of China*

Yanhui Zhang − *College of Chemistry and Chemical Engineering, Xinjiang Key Laboratory of Energy Storage and Photoelectroctalytic Materials, Xinjiang Normal University, Urumqi, Xinjiang 830054, People's Republic of China*

Yanjun Cai − *College of Chemistry and Chemical Engineering, Xinjiang Key Laboratory of Energy Storage and Photoelectroctalytic Materials, Xinjiang Normal University, Urumqi, Xinjiang 830054, People's Republic of China;* orcid.org/0000-0002-7559-1517

He Ren − *College of Chemistry and Chemical Engineering, Xinjiang Key Laboratory of Energy Storage and Photoelectroctalytic Materials, Xinjiang Normal University, Urumqi, Xinjiang 830054, People's Republic of China*

Yingbo Wang − *College of Chemistry and Chemical Engineering, Xinjiang Key Laboratory of Energy Storage and Photoelectroctalytic Materials, Xinjiang Normal University, Urumqi, Xinjiang 830054, People's Republic of China*

Complete contact information is available at: https://pubs.acs.org/10.1021/acs.energyfuels.4c02693

Author Contributions

Kang Tang, writing—review and editing, writing—original draft, and data curation; Hualing Tian, investigation; Yanhui Zhang, software; Yanjun Cai, supervision and conceptualization; He Ren, data analysis; Yingbo Wang, validation; Xiang Yao, writing—review and editing; and Zhi Su, funding acquisition.

Notes

The authors declare no competing financial interest.

■ ACKNOWLEDGMENTS

This study was sponsored by Natural Science Foundation of Xinjiang Uygur Autonomous Region (2022D01B37), Doctoral Research Foundation of Xinjiang Normal University (XJNUBS2309), National Natural Science Foundation of China (22169020), and Xinjiang Key Research and Development Project (2021B01001-1).

REFERENCES

(1) Dunn, B.; Kamath, H.; Tarascon, J. Electrical Energy Storage for the Grid: A Battery of Choices. *Science* **2011**, *334* (6058), 928−935.
(2) Li, M.; Lu, J.; Chen, Z.; Amine, K. 30 Years of Lithium-Ion Batteries. *Adv. Mater.* **2018**, *30* (33), 1800561.
(3) Wang, D.; Bie, X.; Fu, Q.; Dixon, D.; Bramnik, N.; Hu, Y.; Fauth, F.; Wei, Y.; Ehrenberg, H.; Chen, G.; Du, F. Sodium vanadium titanium phosphate electrode for symmetric sodium-ion batteries with high power and long lifespan. *Nat. Commun.* **2017**, *8* (1), 15888.
(4) Nayak, P.; Yang, L.; Brehm, W.; Adelhelm, P. From Lithium-Ion to Sodium-Ion Batteries: Advantages, Challenges, and Surprises. *Angew. Chem., Int. Ed.* **2018**, *57* (1), 102−120.
(5) Usiskin, R.; Lu, Y.; Popovic, J.; Law, M.; Balaya, P.; Hu, Y.-S.; Maier, J. Fundamentals, status and promise of sodium-based batteries. *Nat. Rev. Mater.* **2021**, *6* (11), 1020−1035.
(6) Kim, J.; Kim, H.; Kang, K. Conversion-Based Cathode Materials for Rechargeable Sodium Batteries. *Adv. Energy Mater.* **2018**, *8* (17), 1702646.
(7) Wang, M.; Wang, Q.; Ding, X.; Wang, Y.; Xin, Y.; Singh, P.; Wu, F.; Gao, H. The prospect and challenges of sodium-ion batteries for low-temperature conditions. *Interdiscip. Mater.* **2022**, *1* (3), 373−395.
(8) Hu, Y.; Li, Y. Unlocking Sustainable Na-Ion Batteries into Industry. *ACS Energy Lett.* **2021**, *6* (11), 4115−4117.
(9) Shibata, T.; Fukuzumi, Y.; Kobayashi, W.; Moritomo, Y. Fast discharge process of layered cobalt oxides due to high Na^+ diffusion. *Sci. Rep.* **2015**, *5* (1), 9006.
(10) Zhu, Y.; Xiao, Y.; Dou, S.; Kang, Y.; Chou, S. Spinel/Post-spinel engineering on layered oxide cathodes for sodium-ion batteries. *eScience.* **2021**, *1* (1), 13−27.
(11) Jiang, C.; Wang, Y.; Xin, Y.; Ding, X.; Liu, S.; Pang, Y.; Chen, B.; Wang, Y.; Liu, L.; Wu, F.; Gao, H. Toward high stability of O3-type $NaNi_{1/3}Fe_{1/3}Mn_{1/3}O_2$ cathode material with zirconium substitution for advanced sodium-ion batteries. *Carbon Neutralization.* **2024**, *3* (2), 233−244.
(12) Wang, Q.; Li, J.; Jin, H.; Xin, S.; Gao, H. Prussian-blue materials: Revealing new opportunities for rechargeable batteries. *InfoMater.* **2022**, *4* (6), No. e12311.
(13) Liu, Q.; Meng, X.; Wei, Z.; Wang, D.; Gao, Y.; Wei, Y.; Du, F.; Chen, G. Core/Double-Shell Structured $Na_3V_2(PO_4)_2F_3$@C Nanocomposite as the High Power and Long Lifespan Cathode for Sodium-Ion Batteries. *ACS Appl. Mater. Interfaces.* **2016**, *8* (46), 31709−31715.
(14) Li, H.; Tang, H.; Ma, C.; Bai, Y.; Alvarado, J.; Radhakrishnan, B.; Ong, S.; Wua, F.; Meng, Y.; Wu, C. Understanding the Electrochemical Mechanisms Induced by Gradient Mg^{2+}Distribution of Na-Rich $Na_{3+x}V_{2-x}Mg_x(PO_4)_3$/C for Sodium Ion Batteries. *Chem. Mater.* **2018**, *30* (8), 2498−2505.
(15) Rajagopalan, R.; Zhang, Z.; Tang, Y.; Jia, C.; Ji, X.; Wang, H. Understanding crystal structures, ion diffusion mechanisms and sodium storage behaviors of NASICON materials. *Energy Storage Mater.* **2021**, *34*, 171−193.
(16) Palomares, V.; Casas-Cabanas, M.; Castillo-Martínez, E.; Han, M.; Rojo, T. Update on Na-based battery materials. A growing research path. *Energy Environ. Sci.* **2013**, *6* (8), 2312−2337.
(17) Lv, C.; Lin, C.; Dong, H.; Wei, H.; Yang, J.; Geng, H. Electronic modulation and structure engineered $MoSe_2$ with multi-channel paths as an advanced anode for sodium-ion half/full batteries. *Sci. China Mater.* **2022**, *65* (11), 2997−3006.
(18) Li, J.; Zhao, Q.; Lin, X.; Li, X.; Sheng, H.; Liang, J.; Wu, X.; Yin, Y.; Guo, Y.; Zeng, X. A dynamic polyanion framework with anion/cation co-doping for robust Na/Zn-ion batteries. *J. Power Sources.* **2022**, *530*, 231257.
(19) Barker, J.; Saidi, M.; Swoyer, J. A Sodium-Ion Cell Based on the Fluorophosphate Compound $NaVPO_4F$. *Electrochem. Solid-State Lett.* **2003**, *6* (1), A1.
(20) Fang, C.; Huang, Y.; Zhang, W.; Han, J.; Deng, Z.; Cao, Y.; Yang, H. Routes to High Energy Cathodes of Sodium-Ion Batteries. *Adv. Energy Mater.* **2016**, *6* (5), 1501727.
(21) Bianchini, M.; Brisset, N.; Fauth, F.; Weill, F.; Elkaim, E.; Suard, E.; Masquelier, C.; Croguennec, L. $Na_3V_2(PO_4)_2F_3$ Revisited: A High-Resolution Diffraction Study. *Chem. Mater.* **2014**, *26* (14), 4238−4247.
(22) Zhao, C.; Guo, J.; Gu, Z.; Zhao, X.; Li, W.; Yang, X.; Liang, H.; Wu, X. Robust three-dimensional carbon conductive network in a $NaVPO_4F$ cathode used for superior high-rate and ultralong-lifespan sodium-ion full batteries. *J. Mater. Chem. A.* **2020**, *8* (34), 17454−17462.
(23) Chen, M.; Hua, W.; Xiao, J.; Cortie, D.; Guo, X.; Wang, E.; Gu, Q.; Hu, Z.; Indris, S.; Wang, X.; Chou, S.; Dou, S. Development and Investigation of a NASICON-Type High-Voltage Cathode Material for High-Power Sodium-Ion Batteries. *Angew. Chem., Int. Ed.* **2020**, *59* (6), 2449−2456.
(24) Chen, L.; Zhong, Z.; Ren, S.; Han, D. Carbon-Coated $Na_3V_2(PO_4)_3$ Supported on Multiwalled Carbon Nanotubes for Half-/Full-Cell Sodium-Ion Batteries. *Energy Technol.* **2020**, *8* (3), 1901080.
(25) Mishra, K.; Yadav, N.; Hashmi, S.-A. Recent progress in electrode and electrolyte materials for flexible sodium-ion batteries. *J. Mater. Chem. A.* **2020**, *8* (43), 22507−22543.
(26) Jing, M.; Zhang, J.; Han, C.; Yang, H.; Yao, S.; Zhu, L.; Chen, L.; Xie, Q.; Chen, X.; Shen, X.; Qin, S. A Flexible $Na_3V_2(PO_4)_3$/C Composite Fiber Membrane Cathode for Na-Ion and Na-Li Hybrid-Ion Batteries. *J. Electrochem. Soc.* **2018**, *165* (9), A1761−A1769.
(27) Sun, S.; Chen, Y.; Bai, Q.; Tian, Z.; Huang, Q.; Liu, C.; He, S.; Yang, Y.; Wang, Y.; Guo, L. Unravelling the regulation mechanism of nanoflower shaped $Na_3V_2(PO_4)_3$ in methanol−water system for high performance sodium ion batteries. *Chem. Eng. J.* **2023**, *451* (4), 138780.
(28) Olchowka, J.; Nguyen, L. H. B.; Broux, T.; Sanz Camacho, P.; Petit, E.; Fauth, F.; Carlier, D.; Masquelier, C.; Croguennec, L. Aluminum substitution for vanadium in the $Na_3V_2(PO_4)_2F_3$ and $Na_3V_2(PO_4)_2FO_2$ type materials. *Chem. Commun.* **2019**, *55* (78), 11719−11722.
(29) Nongkynrih, J.; Sengupta, A.; Modak, B.; Mitra, S.; Tyagi, A.-K.; Dutta, D. Enhanced electrochemical properties of W-doped $Na_3V_2(PO_4)_2F_3$@C as cathode material in sodium ion batteries. *Electrochim. Acta.* **2022**, *415*, 140256.
(30) Yi, H.; Ling, M.; Xu, W.; Li, X.; Zheng, Q.; Zhang, H. VSC-doping and VSU-doping of $Na_3V_{2-x}Ti_x(PO_4)_2F_3$ compounds for sodium ion battery cathodes: Analysis of electrochemical performance and kinetic properties. *Nano Energy.* **2018**, *47*, 340−352.
(31) Ma, X.; Yu, X.; Li, X.; Liu, Q.; Liu, Y. Modulating Na vacancies of $Na_4FeV(PO_4)_3$ via Zr-substitution: Toward a superior rate and ultrastable cathode for sodium-ion batteries. *J. Power Sources.* **2022**, *541*, 231727.
(32) Ghosh, S.; Barman, N.; Mazumder, M.; Pati, S. K.; Rousse, G.; Senguttuvan, P. High Capacity and High-Rate NASICON-$Na_{3.75}V_{1.25}Mn_{0.75}(PO_4)_3$ Cathode for Na-Ion Batteries via Modulating Electronic and Crystal Structures. *Adv. Energy Mater.* **2020**, *10* (6), 1902918.
(33) Wang, Z.; Cui, G.; Zheng, Q.; Ren, X.; Yang, Q.; Yuan, S.; Bao, X.; Shu, C.; Zhang, Y.; Li, L.; He, Y.; Chen, L.; Ma, Z.; Liao, X. Ultrafast Charge-Discharge Capable and Long-Life $Na_{3.9}Mn_{0.95}Zr_{0.05}V(PO_4)_3$/C Cathode Material for Advanced Sodium-Ion Batteries. *Small.* **2023**, *19*, 2206987.
(34) Chen, Y.; Liao, X.; Wang, P.; Chen, J.; Zhang, X.; Wu, X.; Smith, S.; Lin, D.; Tan, X.; Zheng, Q. A high-energy-density NASICON-type $Na_3V_{1.25}Ga_{0.75}(PO_4)_3$ cathode with reversible V^{4+}/V^{5+} redox couple for sodium ion batteries. *J. Colloid Interface Sci.* **2024**, *653*, 1−10.
(35) Yue, L.; Peng, C.; Guo, C.; Zhou, X.; Li, G.; Wang, N.; Zhang, J.; Liu, J.; Bai, Z.; Song Zhao, X. $Na_3V_{2-x}Fe_x(PO_4)_2O_2F$: An advanced cathode material with ultra-high stability for superior sodium storage. *Chem. Eng. J.* **2022**, *441*, 136132.
(36) Bin, D.; Wang, Y.; Tamirat, A.-G.; Zhu, P.; Yang, B.; Wang, J.; Huang, J.; Xia, Y. Stable High-Voltage Aqueous Zinc Battery Based on

https://doi.org/10.1021/acs.energyfuels.4c02693
Energy Fuels 2024, 38, 18035−18043

Carbon-Coated $NaVPO_4F$ Cathode. *ACS Sustainable Chem. Eng.* **2021**, *9* (8), 3223−3231.
(37) Feng, P.; Wang, W.; Hou, J.; Wang, K.; Cheng, S.; Jiang, K. A 3D coral-like structured $NaVPO_4F/C$ constructed by a novel synthesis route as high-performance cathode material for sodium-ion battery. *Chem. Eng. J.* **2018**, *353*, 25−33.
(38) Li, M.; Sun, C.; Ni, Q.; Sun, Z.; Liu, Y.; Li, Y.; Li, L.; Jin, H.; Zhao, Y. High Entropy Enabling the Reversible Redox Reaction of V^{4+}/V^{5+} Couple in NASICON-Type Sodium Ion Cathode. *Adv. Energy Mater.* **2023**, *13* (12), 2203971.
(39) Puspitasari, D. A.; Patra, J.; Hung, I.; Bresser, D.; Lee, T.; Chang, J. Optimizing the Mg Doping Concentration of $Na_3V_{2-x}Mg_x(PO_4)_2F_3/C$ for Enhanced Sodiation/Desodiation Properties. *ACS Sustainable Chem. Eng.* **2021**, *9* (20), 6962−6971.
(40) Puspitasari, D. A.; Patra, J.; Hernandha, R. F. H.; Chiang, Y.-S.; Inoishi, A.; Chang, B. K.; Lee, T.-C.; Chang, J.-K. Enhanced Electrochemical Performance of Ca-Doped $Na_3V_2(PO_4)_2F_3/C$ Cathode Materials for Sodium-Ion Batteries. *ACS Appl. Mater. Interfaces.* **2024**, *16* (1), 496−506.
(41) Ling, M.; Jiang, Q.; Li, T.; Wang, C.; Lv, Z.; Zhang, H.; Zheng, Q.; Li, X. The Mystery from Tetragonal $NaVPO_4F$ to Monoclinic $NaVPO_4F$: Crystal Presentation, Phase Conversion, and Na-Storage Kinetics. *Adv. Energy Mater.* **2021**, *11* (21), 2100627.
(42) Jin, T.; Liu, Y.; Li, Y.; Cao, K.; Wang, X.; Jiao, L. Electrospun $NaVPO_4F/C$ Nanofibers as Self-Standing Cathode Material for Ultralong Cycle Life Na-Ion Batteries. *Adv. Energy Mater.* **2017**, *7* (15), 1700087.
(43) Law, M.; Balaya, P. $NaVPO_4F$ with high cycling stability as a promising cathode for sodium-ion battery. *Energy Storage Mater.* **2018**, *10*, 102−113.
(44) Rudola, A.; Aurbach, D.; Balaya, P. A new phenomenon in sodium batteries: Voltage step due to solvent interaction. *Electrochem. Commun.* **2014**, *46*, 56−59.
(45) Hu, E.; Bak, S.-M.; Liu, Y.; Liu, J.; Yu, X.; Zhou, Y.; Zhou, J.; Khalifah, P.; Ariyoshi, K.; Nam, K.-W.; Yang, X.-Q. Utilizing Environmental Friendly Iron as a Substitution Element in Spinel Structured Cathode Materials for Safer High Energy Lithium-Ion Batteries. *Adv. Energy Mater.* **2016**, *6* (3), 1501662.
(46) Cheng, B.; Zhang, S.; Zou, F.; Luo, L.; Chen, Y.; Chen, S.; Zhuo, H.; Zeng, X. Nano-$NaVPO_4F$ enwrapped in reduced graphene oxide as a cathode material for long-cycle and high-rate sodium-ion batteries. *J. Alloys Compd.* **2019**, *811*, 151828.
(47) Saravanan, K.; Mason, C. W.; Rudola, A.; Wong, K. H.; Balaya, P. The First Report on Excellent Cycling Stability and Superior Rate Capability of $Na_3V_2(PO_4)_3$ for Sodium Ion Batteries. *Adv. Energy Mater.* **2013**, *3* (4), 444−450.
(48) Guo, J.-Z.; Wu, X.-L.; Wan, F.; Wang, J.; Zhang, X.-H.; Wang, R.-S. A Superior $Na_3V_2(PO_4)_3$-Based Nanocomposite Enhanced by Both N-Doped Coating Carbon and Graphene as the Cathode for Sodium-Ion Batteries. *Chem. - Eur. J.* **2015**, *21* (48), 17371−17378.
(49) Xiong, H.; Liu, Y.; Yang, Y.; Shao, H. Carbon-Polytetrahydrofuran Double-Coated $Na_3V_2(PO_4)_2F_3$ Submicron-Composite as High-Energy/Power Cathode Material for Sodium Metal Battery. *J. Electrochem. Soc.* **2018**, *165* (5), A746.
(50) Li, H.; Jin, T.; Chen, X.; Lai, Y.; Zhang, Z.; Bao, W.; Jiao, L. Rational Architecture Design Enables Superior Na Storage in Greener NASICON-$Na_4MnV(PO_4)_3$ Cathode. *Adv. Energy Mater.* **2018**, *8* (24), 1801418.
(51) Zhu, Q.; Wu, J.; Li, W.; Hu, X.; Tian, N.; He, Li.; Li, Y. Potassium doping improves the electrochemical performance of $Na_4MnCr(PO_4)_3$ cathode for sodium-ion batteries. *Appl. Surf. Sci.* **2024**, *652* (15), 159320.
(52) Wei, Q.; DeBlock, R.-H.; Butts, D.-M.; Choi, C.; Dunn, B. Pseudocapacitive Vanadium-based Materials toward High-Rate Sodium-Ion Storage. *Energy Environ. Mater.* **2020**, *3* (3), 221−234.
(53) Ling, M.; Li, F.; Yi, H.; Li, X.; Hou, G.; Zheng, Q.; Zhang, H. 2018. Superior Na-storage performance of molten-state-blending-synthesized monoclinic $NaVPO_4F$ nanoplates for Na-ion batteries. *J. Mater. Chem. A.* **2018**, *6* (47), 24201−24209.
(54) Wang, Y.; Bin, D.; Wang, C.; Cao, Y.; Xia, Y. Carbon-Coated $NaVPO_4F$ as a High-Capacity Cathode for Aqueous Sodium-Ion Battery. *Batteries Supercaps.* **2023**, *6* (10), No. e202300275.
(55) Kumar, V.; Ghosh, S.; Biswas, S.; Martha, S. Pitch-Derived Soft-Carbon-Wrapped $NaVPO_4F$ Composite as a Potential Cathode Material for Sodium-Ion Batteries. *ACS Appl. Energy Mater.* **2021**, *4* (4), 4059−4069.

https://doi.org/10.1021/acs.energyfuels.4c02693
Energy Fuels 2024, 38, 18035−18043